

Observation of multiple nodal lines in SmSbTe

Sabin Regmi^{1,*}, Gyanendra Dhakal^{1,*}, Fairoja Cheenicode Kabeer², Neil Harrison³, Firoza Kabir¹, Anup Pradhan Sakhya¹, Krzysztof Gofryk⁴, Dariusz Kaczorowski⁵, Peter M. Oppeneer², and Madhab Neupane^{1,†}

¹Department of Physics, University of Central Florida, Orlando, Florida 32816, USA

²Department of Physics and Astronomy, Uppsala University, P.O. Box 516, S-75120 Uppsala, Sweden

³National High Magnetic Field Laboratory, Los Alamos, New Mexico 87545, USA

⁴Idaho National Laboratory, Idaho Falls, Idaho 83415, USA

⁵Institute of Low Temperature and Structure Research, Polish Academy of Sciences, ul. Okólna 2, 50-422 Wrocław, Poland



(Received 1 August 2021; accepted 14 February 2022; published 9 March 2022)

Having been a ground for various topological fermionic phases, the family of ZrSiS-type 111 materials has been under experimental and theoretical investigations. Within this family of materials, the subfamily Ln SbTe (Ln = lanthanide elements) is gaining interest in recent times as the strong correlation effects and magnetism arising from the $4f$ electrons of the lanthanides can provide an important platform to study the link between topology, magnetism, and correlation. In this Letter, we report the systematic study of the electronic structure of SmSbTe—a member of the Ln SbTe subfamily—by utilizing angle-resolved photoemission spectroscopy in conjunction with first-principles calculations, transport, and magnetic measurements. Our experimental results identify multiple Dirac nodes forming the nodal lines along the Γ - X and Z - R directions in the bulk Brillouin zone (BZ) as predicted by our theoretical calculations. A surface Dirac-like state is also observed at the \bar{X} point of the surface BZ. Our study highlights SmSbTe as a promising candidate to understand the topological electronic structure of Ln SbTe materials.

DOI: 10.1103/PhysRevMaterials.6.L031201

Introduction. The field of topological quantum materials has been growing ever since the discovery of three-dimensional (3D) topological insulators [1–4]. Following the inflow of theoretical and experimental research studies in the field, topological semimetals including the Dirac semimetals [5,6], Weyl semimetals [7,8], nodal-line/loop semimetals (NLSMs) [9–11], and beyond [12,13] were discovered. After the discovery of the nodal-line topological state in ZrSiS [10,11], the ZrSiS-type 111 materials have attracted a lot of research interests. The materials in this family are shown to host nonsymmorphic topological fermions coming from the square-net plane of the group-IV elements (Si, Ge, Sb) and nodal-line fermions [10,11,14–23]. The existence of exotic phenomena such as unconventional magnetotransport behavior [24–27], flat optical conductivity [28], unconventional mass enhancement [29], etc., reported in this family of materials enticed studies of more members of this family of materials.

Among various materials in this family, materials with a Si-square net have been extensively studied [10,11,14–18,21,23], however studies on Sb-square-net materials under this family are still limited. Among them, the materials under the subfamily Ln SbTe (Ln = lanthanide elements) could be of particular interest because of the potential co-existence of topology with magnetic ordering carried by the lanthanides.

Furthermore, the lanthanide elements come with strongly correlated $4f$ electrons, which can potentially give a way to study the interplay between topology, correlation, and magnetism in the ZrSiS-type materials. This makes the study of the detailed electronic structure of Ln SbTe-type materials desirable, however, only a few studies have been carried out to date. GdSbTe is reported to exhibit a topological nodal-line state as well as an antiferromagnetic Dirac state protected by the combination of broken time-reversal symmetry and rotoinversion symmetry by using angle-resolved photoemission spectroscopy (ARPES) [30]. Because of the tunability of the magnetic ordering of the Ce $4f$ electrons, CeSbTe is reported to host a variety of topological features in the electronic structure [31]. Another study on CeSbTe showed that the stronger spin-orbit coupling (SOC) in this material creates a more symmetric Dirac cone which is protected by the nonsymmorphic symmetry [32]. The nodal-line state in HoSbTe is gapped out in the order of hundreds of meV which can be directly observed via ARPES [33]. NdSbTe has been shown to exhibit a coexistence of metamagnetic transitions and possible Kondo localization [34], while the Kondo mechanism has been reported in CeSbTe [35]. LaSbTe has been identified as a genuine NLSM with the nodal-line state present even with the inclusion of the SOC effect [36]. Despite all these works on Ln SbTe, the Sm variant of this family has not been studied yet. The study of this compound will be useful not only to uncover the underlying electronic structure, but also to understand the interplay of the topological states and the nodal-band gaps in Ln SbTe with lanthanide element substitution.

*These authors contributed equally to this work.

†Corresponding author: madhab.neupane@ucf.edu

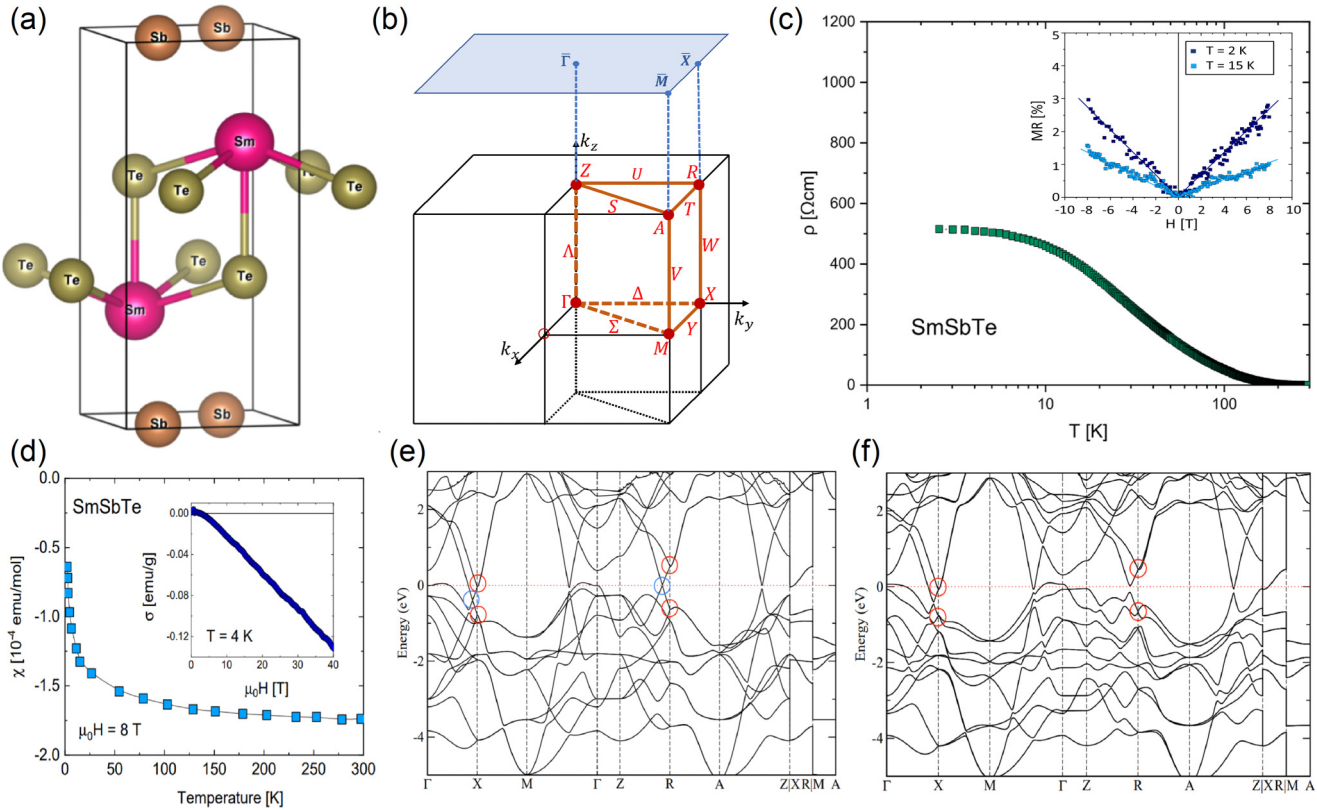


FIG. 1. Crystal structure and sample characterization of SmSbTe. (a) Unit cell of the SmSbTe crystal structure. (b) Bulk Brillouin zone and the projected surface Brillouin zone with the high-symmetry points marked. (c) The temperature dependence of electrical resistivity of the SmSbTe crystal. The inset shows the magnetic field dependence of the magnetoresistance. The solid lines are a guide for the eye. (d) Temperature dependence of magnetic susceptibility measured in 8 T. The inset shows the field dependence of magnetization measured up to 40 T. (e), (f) Calculated bulk band structures without and with the consideration of the effects of SOC, respectively.

In this Letter, we report a systematic ARPES study of SmSbTe with parallel first-principles calculations, transport, and magnetic measurements in order to uncover the underlying electronic structure, topology, and magnetism in this compound. The low-temperature electronic structure reported in our study shows the presence of a typical ZrSiS-type diamond-shaped Fermi surface (FS) formed by the nodal-line states. Our experimental observations reveal multiple Dirac nodes along the bulk Γ - X and Z - R directions that form the nodal lines in concurrence with the theoretical calculations. Furthermore, the experimental results reveal the presence of a Dirac-like state around the \bar{X} point of the surface Brillouin zone (BZ). Our study provides another variant in order to understand the underlying low-temperature electronic structure in the Ln SbTe materials.

Methods. Single crystals of SmSbTe were grown using the flux method and characterized as explained in the Supplemental Material (SM) [37]. Electrical resistance, magnetoresistance, and magnetic susceptibility (VSM) were measured from 2 to 300 K in magnetic fields up to 14 T using a Quantum Design DynaCool-14 System. Magnetization measurements in pulsed magnetic fields up to 40 T were measured using a pickup-coil technique at NHMFL, Los Alamos. Synchrotron-based ARPES measurements were performed at the SLS SIS-X09LA BL at a temperature of 20 K with the experimental energy resolution of the setup set better than 20 meV. The first-principles calculations were performed

within the density-functional theory (DFT) formalism [38,39] on the basis of the projector augmented-wave potential [40] using the Vienna *ab initio* simulation package (VASP) [41,42]. For more details, see Sec. I of the SM [37].

Results. SmSbTe is a PbFCl-type telluride that crystallizes in a tetragonal layered crystal structure with $P4/nmm$ (No. 129) nonsymmorphic space group. The Sb square plane is sandwiched by the Sm-Te layers forming the quintuple layers of Te-Sm-Sb-Sm-Te slabs along the [001] directions. Each quintuple layer is weakly bonded with the neighboring layers via van der Waals interactions, therefore the crystals usually cleave at the Te termination on the (001) plane. Each layer of atoms in this crystal supports global C_{4v} symmetry. Since the Sb layer acts as a glide mirror plane, it breaks the C_{4v} symmetry locally at the Sb atom sites, which is in line with the $(M_z | \frac{1}{2} \frac{1}{2} 0)$ symmetry operation. A unit cell for the SmSbTe crystal structure is presented in Fig. 1(a). The theoretically optimized lattice constants are $a = b = 4.338 \text{ \AA}$ and $c = 9.398 \text{ \AA}$. The 3D bulk BZ is presented in Fig. 1(b) where the high-symmetry points are indicated. The bulk BZ is projected onto the (001) surface on which the ARPES measurements are performed. The electrical resistivity of the SmSbTe crystals is plotted against the temperature in Fig. 1(c). Interestingly, the resistivity of SmSbTe strongly increases upon cooling and then saturates at $\sim 8 \text{ K}$. It has been shown that in many systems with surface Dirac states, the saturation of the resistance occurs below temperatures where the metallic topological

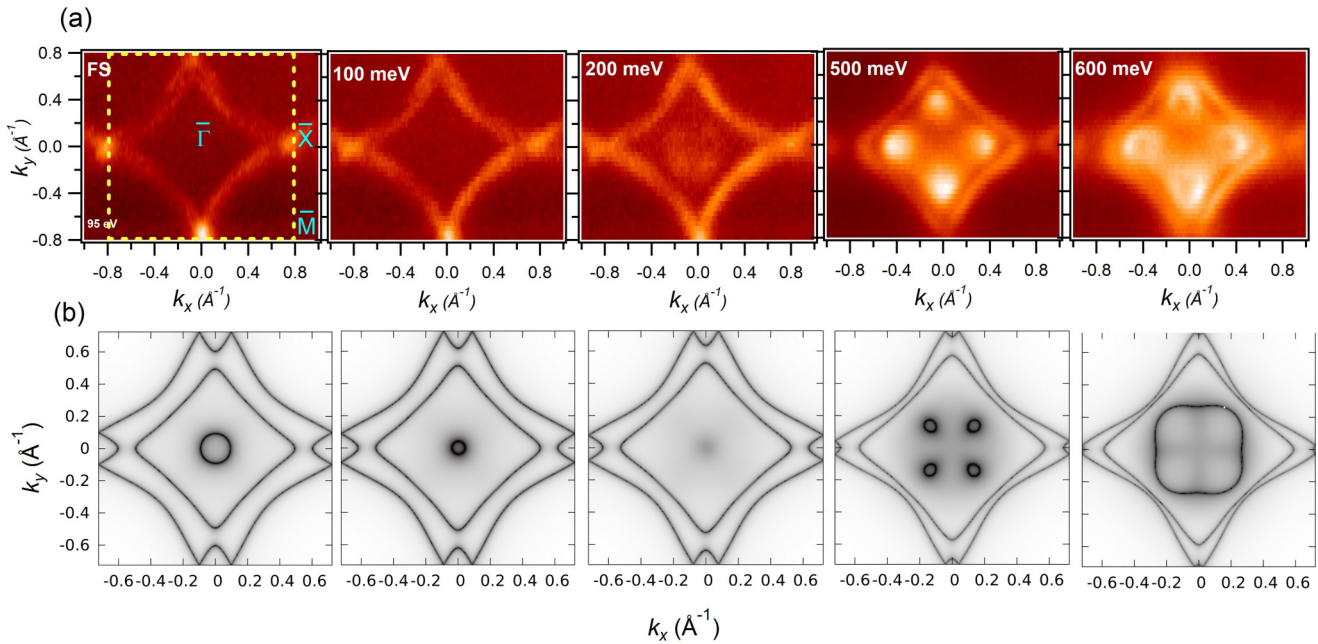


FIG. 2. Fermi map and constant energy contours. (a) ARPES measured Fermi surface (top leftmost) and constant energy contours at various binding energies below the Fermi energy on the (001) surface of SmSbTe. The yellow-dashed square on the FS plot represents the surface Brillouin zone. Corresponding binding energies are marked on each of the constant energy contour plots. (b) Calculated Fermi map and constant energy contours corresponding to (a). ARPES data were collected at the SIS-HRPES end station at the SLS, PSI with a photon energy of 95 eV and at a temperature of 20 K.

surface state resistance starts to dominate over the strongly increasing bulk resistance, even for bulk crystals [43,44]. The magnetoresistance (MR) plotted in the inset of Fig. 1(c) shows a linear field dependency, which signals towards the possible linear dispersion in the low-temperature electronic structure. The magnetic susceptibility presented in Fig. 1(d) shows typical characteristics of weak diamagnetism. The $\chi(T)$ curve is negative and nearly temperature independent and the magnetization measured in magnetic fields up to 45 T shows a negative slope of $M(H)$, typical for diamagnetic materials [see the inset of Fig. 1(d)]. The calculated bulk band structures without and with the inclusion of SOC are shown in Figs. 1(e) and 1(f), respectively. In the presence of SOC, the Sm d and Sb p bands along the Z-A direction couple together resulting in band inversion and gap opening, indicating the nontrivial topology in SmSbTe (see SM [37]). The calculations suggest that in the absence of SOC, multiple Dirac nodal lines are present along different high-symmetry directions as indicated by red and blue circles in Fig. 1(e). Some of these Dirac nodal lines are gapped out when the effect of SOC is taken into account with a significant gap size especially along the Z-R direction [see Fig. 1(f)]. A similar SOC gap opening was recently reported in HoSbTe [33]. On the other hand, some Dirac nodal lines remain robust even in the presence of SOC [see the red circles in Fig. 1(f)].

In order to investigate the detailed electronic structure of SmSbTe, we present the experimentally obtained constant energy contours at the Fermi energy (top leftmost plot) and at various binding energies measured with a photon energy of 95 eV, which corresponds to $k_z = 0$ (see SM for k_z -dependent measurements [37]). The Fermi surface is typical of ZrSiS-

type materials with a diamond-shaped Fermi pocket centered at the $\bar{\Gamma}$ point. At around 200 meV below the Fermi level, a faint circular feature begins to appear around the $\bar{\Gamma}$ point. This circular feature grows in its size on moving to higher binding energies and emerges into a second diamond-shaped energy pocket at around 500 meV below the Fermi level. The corners of this second diamond-shaped feature are surrounded by small circular pockets at this binding energy. These circular pockets evolve with binding energy and become clear ringlike pockets around 600 meV below the Fermi level. Figure 2(b) shows the calculated Fermi map and constant energy contours corresponding to Fig. 2(a). The calculated constant energy contours match well with the experimental plots. The features seen at the $\bar{\Gamma}$ point near the Fermi level in calculated maps are absent in the experimental plots, which is probably due to matrix element effects. Even though the diamond-shaped Fermi surface resembles a single sheet in this photon energy which appears similar to the other two Ln SbTe compounds [30,36], the Fermi map obtained at a low photon energy (35 eV) clearly depicts a double-sheet diamond shape [37].

In Fig. 3, we present the ARPES measured dispersion maps along the $\bar{M}-\bar{\Gamma}-\bar{M}$ and $\bar{X}-\bar{\Gamma}-\bar{X}$ directions, respectively, at two different k_z planes. Figure 3(a) displays the dispersion map along the $\bar{M}-\bar{\Gamma}-\bar{M}$ direction at $k_z = 0$. A linearly dispersing band seems to cross the Fermi level, which gives rise to the diamond-shaped Fermi pocket. Even though bulk band calculations suggest a gapped state without and with SOC along this direction, we cannot resolve the gap in our experimental data probably because of the experimental gap being beyond our experimental resolution. The separation of the bands forming the gapped state may be very close, therefore they

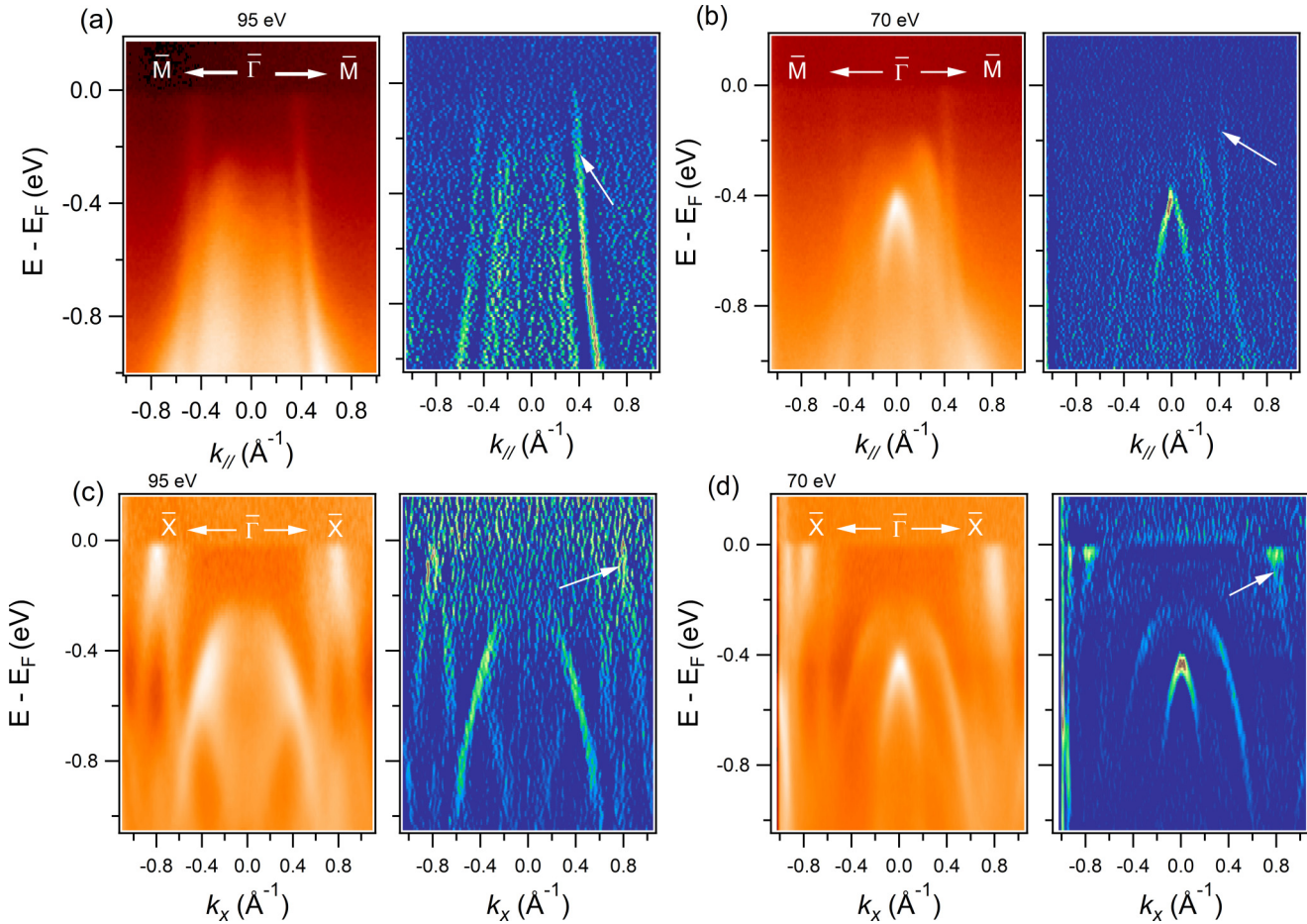


FIG. 3. Observation of a nodal-line semimetal in SmSbTe. (a) Dispersion map and its second derivatives along the $\bar{M}-\bar{\Gamma}-\bar{M}$ direction measured at $k_z = 0$. (b) Dispersion map and its second derivatives along the $\bar{M}-\bar{\Gamma}-\bar{M}$ direction measured at $k_z = \pi$. (c) Dispersion map and its second derivative along the $\bar{X}-\bar{\Gamma}-\bar{X}$ direction measured at $k_z = 0$. (d) Dispersion map and its second derivative along the $\bar{M}-\bar{\Gamma}-\bar{M}$ direction measured at $k_z = \pi$. ARPES data were collected at the SIS-HRPES end station at the SLS, PSI at a temperature of 20 K.

seem to be a single band over a large energy range (≥ 1 eV) in the vicinity of Fermi level. Next, we present a dispersion map along the $\bar{M}-\bar{\Gamma}-\bar{M}$ direction at $k_z = \pi$ in Fig. 3(b). The bands along this direction show significant changes with photon energies indicating the bulk nature of the bands. Figure 3(c) presents a dispersion map ($k_z = 0$) along the $\bar{X}-\bar{\Gamma}-\bar{X}$ direction which depicts linearly dispersing bands in the vicinity of \bar{X} . Those bands form a nodal line as predicted by bulk-band calculations. We can see that the Dirac-like crossing lies very close to the Fermi level. The holelike bands away from the Fermi level around the $\bar{\Gamma}$ make a circular feature at constant energy contours as seen in Fig. 2(a). In Fig. 3(d), the dispersion map along the $\bar{X}-\bar{\Gamma}-\bar{X}$ ($k_z = \pi$) is presented, which shows the presence of Dirac-like bands forming the nodal-line state in the bulk calculation along the $Z-R$ direction [Fig. 1(f)]. The dispersion maps along these two different directions at two photon energies provide the indication of the bulk bands at the $\bar{\Gamma}$ point, whereas we can clearly see the coexistence of surface and bulk bands in the vicinity of \bar{X} .

Next, we focus on the dispersion map along the $\bar{M}-\bar{X}-\bar{M}$ direction which shows the Dirac-like dispersion (Fig. 4). The bands forming the Dirac-like dispersion do not disperse with the photon energies, indicating that the bands correspond to the surface (see SM [37] for more photon energy-dependent

measurements). The Dirac node exists around 600 meV below the Fermi level. Figure 4(b) displays the surface calculation along the $\bar{M}-\bar{X}-\bar{M}$ direction, which exhibits a small gap at the Dirac node. This gap might be due to the quantum size effects that can occur in slab calculations [11]. The experimental gap, if there is any, is not resolved, which is likely due to the experimental resolution being greater than the gap size.

Conclusion. In summary, we performed a detailed ARPES study on SmSbTe together with transport and magnetic measurements as well as first-principles calculations. Our ARPES data show the typical ZrSiS-type diamond Fermi surface and Dirac-like states at the corner of the BZ. The surface Dirac-like state at the \bar{X} point in the surface BZ is gapped according to our theoretical calculations, however the gap is too small to be resolved from our experiments. Multiple Dirac nodes forming the nodal-line states are present along different high-symmetry directions in the absence of SOC, some of which are gapped out and the others remain robust in the presence of SOC. In addition, we observe the saturation of the electrical resistivity at low temperatures and linear magnetoresistance through our transport measurements. Our study provides another platform in order to understand the electronic structure in Ln SbTe subfamily of materials.

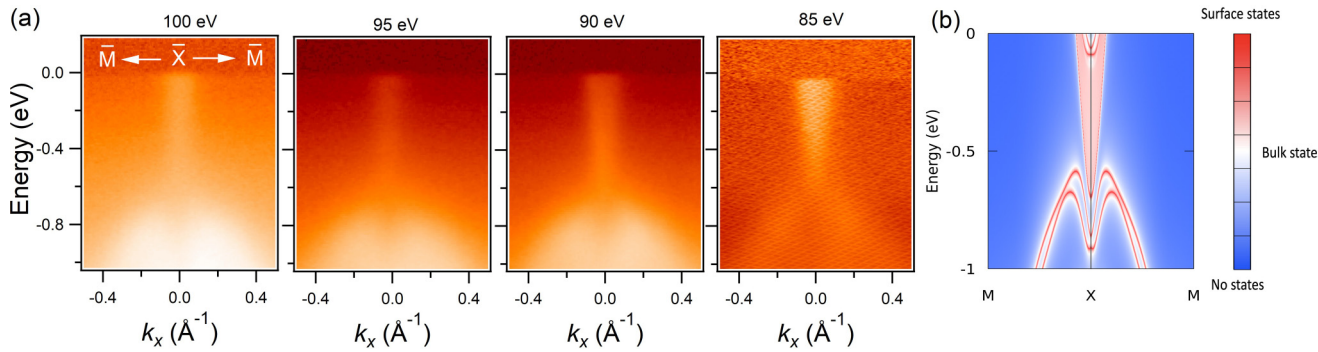


FIG. 4. Observation of the surface state on the (001) surface of SmSbTe. (a) Dispersion maps along the $\bar{M}-\bar{X}-\bar{M}$ direction measured at different photon energies. The corresponding photon energies are noted on top of each plot. (b) Calculated surface electronic structure along the $\bar{M}-\bar{X}-\bar{M}$. ARPES data were collected at the SIS-HRPES end station at the SLS, PSI at a temperature of 20 K.

Note added. Recently, we became aware of a work on the same material system [51].

Acknowledgments. M.N. acknowledges support from the National Science Foundation (NSF) CAREER Award No. DMR-1847962, the Air Force Office of Scientific Research under Award No. FA9550-17-1-0415, the Air Force Office of Scientific Research MURI Grant No. FA9550-20-1-0322, and the Center for Thermal Energy Transport under Irradiation, an Energy Frontier Research Center funded by the U.S. DOE, Office of Basic Energy Sciences. P.M.O. acknowledges support from the Swedish Research Council (VR) and the Knut and Alice Wallenberg Foundation (Grant No. 2015.0060). Computational resources were provided by the Swedish National Infrastructure for Computing (SNIC)

(Grant No. 2018-05973). K.G. acknowledges support from the INL Laboratory Directed Research and Development (LDRD) Program under DOE Idaho Operations Office Contract DE-AC07-05ID14517. N.H. acknowledges support from the U.S. DOE Basic Energy Science program through the project “Science at 100T” at LANL. A portion of this work was performed at the National High Magnetic Field Laboratory, which is supported by the National Science Foundation Cooperative Agreement No. DMR-1644779 and the state of Florida. D.K. was supported by the National Science Centre (Poland) under Research Grant No. 2021/41/B/ST3/01141. We are grateful to Nicholas Clark Plumb, Ming Shi, Hang Li, and Sailong Ju for beamline assistance at PSI, SLS.

- [1] M. Z. Hasan and C. L. Kane, Colloquium: Topological insulators, *Rev. Mod. Phys.* **82**, 3045 (2010).
- [2] X.-L. Qi and S.-C. Zhang, Topological insulators and superconductors, *Rev. Mod. Phys.* **83**, 1057 (2011).
- [3] M. Z. Hasan, S.-Y. Xu, and M. Neupane, in *Topological Insulators: Fundamentals and Perspectives*, edited by S. R. F. Ortmann and S. O. Valenzuela (Wiley, Hoboken, NJ, 2015).
- [4] A. Bansil, H. Lin, and T. Das, Colloquium: Topological band theory, *Rev. Mod. Phys.* **88**, 021004 (2016).
- [5] N. P. Armitage, E. J. Mele, and A. Vishwanath, Weyl and Dirac semimetals in three-dimensional solids, *Rev. Mod. Phys.* **90**, 015001 (2018).
- [6] M. Neupane, S.-Y. Xu, R. Sankar, N. Alidoust, G. Bian, C. Liu, I. Belopolski, T.-R. Chang, H.-T. Jeng, H. Lin, A. Bansil, F. Chou, and M. Z. Hasan, Observation of a three-dimensional topological Dirac semimetal phase in high-mobility Cd₃As₂, *Nat. Commun.* **5**, 3786 (2014).
- [7] S.-Y. Xu, I. Belopolski, N. Alidoust, M. Neupane, G. Bian, C. Zhang, R. Sankar, G. Chang, Z. Yuan, C.-C. Lee, S.-M. Huang, H. Zheng, J. Ma, D. S. Sanchez, B. Wang, A. Bansil, F. Chou, P. P. Shibayev, H. Lin, S. Jia *et al.*, Discovery of a Weyl fermion semimetal and topological Fermi arcs, *Science* **349**, 613 (2015).
- [8] B. Q. Lv, H. M. Weng, B. B. Fu, X. P. Wang, H. Miao, J. Ma, P. Richard, X. C. Huang, L. X. Zhao, G. F. Chen, Z. Fang, X. Dai, T. Qian, and H. Ding, Experimental Dis-
- covery of Weyl Semimetal TaAs, *Phys. Rev. X* **5**, 031013 (2015).
- [9] A. A. Burkov, M. D. Hook, and L. Balents, Topological nodal semimetals, *Phys. Rev. B* **84**, 235126 (2011).
- [10] L. M. Schoop, M. N. Ali, C. Straßer, A. Topp, A. Varykhalov, D. Marchenko, V. Duppel, S. S. P. Parkin, B. V. Lotsch, and C. R. Ast, Dirac cone protected by non-symmorphic symmetry and three-dimensional Dirac line node in ZrSiS, *Nat. Commun.* **7**, 11696 (2016).
- [11] M. Neupane, I. Belopolski, M. M. Hosen, D. S. Sanchez, R. Sankar, M. Szlawska, S.-Y. Xu, K. Dimitri, N. Dhakal, P. Maldonado, P. M. Oppeneer, D. Kaczorowski, F. Chou, M. Z. Hasan, and T. Durakiewicz, Observation of topological nodal fermion semimetal phase in ZrSiS, *Phys. Rev. B* **93**, 201104(R) (2016).
- [12] B. Bradlyn, J. Cano, Z. Wang, M. G. Vergniory, C. Felser, R. J. Cava, and B. A. Bernevig, Beyond Dirac and Weyl fermions: Unconventional quasiparticles in conventional crystals, *Science* **353**, aaf5037 (2016).
- [13] D. S. Sanchez, I. Belopolski, T. A. Cochran, X. Xu, J.-X. Yin, G. Chang, W. Xie, K. Manna, V. Süß, C.-Y. Huang, N. Alidoust, D. Multer, S. S. Zhang, N. Shumiya, X. Wang, G.-Q. Wang, T.-R. Chang, C. Felser, S.-Y. Xu, S. Jia, H. Lin *et al.*, Topological chiral crystals with helicoid-arc quantum states, *Nature (London)* **567**, 500 (2019).

[14] A. Topp, J. M. Lippmann, A. Varykhalov, V. Duppel, B. V. Lotsch, C. R. Ast, and L. M. Schoop, Non-symmorphic band degeneracy at the Fermi level in ZrSiTe, *New J. Phys.* **18**, 125014 (2016).

[15] J. Hu, Z. Tang, J. Liu, X. Liu, Y. Zhu, D. Graf, K. Myhro, S. Tran, C. N. Lau, J. Wei, and Z. Mao, Evidence of Topological Nodal-Line Fermions in ZrSiSe and ZrSiTe, *Phys. Rev. Lett.* **117**, 016602 (2016).

[16] D. Takane, Z. Wang, S. Souma, K. Nakayama, C. X. Trang, T. Sato, T. Takahashi, and Y. Ando, Dirac-node arc in the topological line-node semimetal HfSiS, *Phys. Rev. B* **94**, 121108(R) (2016).

[17] M. M. Hosen, K. Dimitri, I. Belopolski, P. Maldonado, R. Sankar, N. Dhakal, G. Dhakal, T. Cole, P. M. Oppeneer, D. Kaczorowski, F. Chou, M. Z. Hasan, T. Durakiewicz, and M. Neupane, Tunability of the topological nodal-line semimetal phase in ZrSiX-type materials ($X = \text{S, Se, Te}$), *Phys. Rev. B* **95**, 161101(R) (2017).

[18] C. Chen, X. Xu, J. Jiang, S. C. Wu, Y. P. Qi, L. X. Yang, M. X. Wang, Y. Sun, N. B. M. Schröter, H. F. Yang, L. M. Schoop, Y. Y. Lv, J. Zhou, Y. B. Chen, S. H. Yao, M. H. Lu, Y. F. Chen, C. Felser, B. H. Yan, Z. K. Liu, and Y. L. Chen, Dirac line nodes and effect of spin-orbit coupling in the nonsymmorphic critical semimetals $MSiS$ ($M = \text{Hf, Zr}$), *Phys. Rev. B* **95**, 125126 (2017).

[19] R. Lou, J. Z. Ma, Q. N. Xu, B. B. Fu, L. Y. Kong, Y. G. Shi, P. Richard, H. M. Weng, Z. Fang, S. S. Sun, Q. Wang, H. C. Lei, T. Qian, H. Ding, and S. C. Wang, Emergence of topological bands on the surface of ZrSnTe crystal, *Phys. Rev. B* **93**, 241104(R) (2016).

[20] J. Hu, Y. Zhu, X. Gui, D. Graf, Z. Tang, W. Xie, and Z. Mao, Quantum oscillation evidence for a topological semimetal phase in ZrSnTe, *Phys. Rev. B* **97**, 155101 (2018).

[21] J. Zhang, M. Gao, J. Zhang, X. Wang, X. Zhang, M. Zhang, W. Niu, R. Zhang, and Y. Xu, Transport evidence of 3D topological nodal-line semimetal phase in ZrSiS, *Front. Phys.* **13**, 137201 (2018).

[22] M. M. Hosen, K. Dimitri, A. Aperis, P. Maldonado, I. Belopolski, G. Dhakal, F. Kabir, C. Sims, M. Z. Hasan, D. Kaczorowski, T. Durakiewicz, P. M. Oppeneer, and M. Neupane, Observation of gapless Dirac surface states in ZrGeTe, *Phys. Rev. B* **97**, 121103(R) (2018).

[23] B. B. Fu, C. J. Yi, T. T. Zhang, M. Caputo, J. Z. Ma, X. Gao, B. Q. Lv, L. Y. Kong, Y. B. Huang, P. Richard, M. Shi, V. N. Strocov, C. Fang, H. M. Weng, Y. G. Shi, T. Qian, and H. Ding, Dirac nodal surfaces and nodal lines in ZrSiS, *Sci. Adv.* **5**, eaau6459 (2019).

[24] M. N. Ali, L. M. Schoop, C. Garg, J. M. Lippmann, E. Lara, B. Lotsch, and S. S. P. Parkin, Butterfly magnetoresistance, quasi-2D Dirac Fermi surface and topological phase transition in ZrSiS, *Sci. Adv.* **2**, e1601742 (2016).

[25] Y.-Y. Lv, B.-B. Zhang, X. Li, S.-H. Yao, Y. B. Chen, J. Zhou, S.-T. Zhang, M.-H. Lu, and Y.-F. Chen, Extremely large and significantly anisotropic magnetoresistance in ZrSiS single crystals, *Appl. Phys. Lett.* **108**, 244101 (2016).

[26] R. Singha, A. K. Pariari, B. Satpati, and P. Mandal, Large non-saturating magnetoresistance and signature of nondegenerate Dirac nodes in ZrSiS, *Proc. Natl. Acad. Sci. USA* **114**, 2468 (2017).

[27] N. Kumar, K. Manna, Y. Qi, S.-C. Wu, L. Wang, B. Yan, C. Felser, and C. Shekhar, Unusual magnetotransport from Si-square nets in topological semimetal HfSiS, *Phys. Rev. B* **95**, 121109(R) (2017).

[28] M. B. Schilling, L. M. Schoop, B. V. Lotsch, M. Dressel, and A. V. Pronin, Flat Optical Conductivity in ZrSiS due to Two-Dimensional Dirac Bands, *Phys. Rev. Lett.* **119**, 187401 (2017).

[29] S. Pezzini, M. R. van Delft, L. M. Schoop, B. V. Lotsch, A. Carrington, M. I. Katsnelson, N. E. Hussey, and S. Wiedmann, Unconventional mass enhancement around the Dirac nodal loop in ZrSiS, *Nat. Phys.* **14**, 178 (2018).

[30] M. M. Hosen, G. Dhakal, K. Dimitri, P. Maldonado, A. Aperis, F. Kabir, C. Sims, P. Riseborough, P. M. Oppeneer, D. Kaczorowski, T. Durakiewicz, and M. Neupane, Discovery of topological nodal-line fermionic phase in a magnetic material GdSbTe, *Sci. Rep.* **8**, 13283 (2018).

[31] L. M. Schoop, A. Topp, J. Lippmann, F. Orlandi, L. Müchler, M. G. Vergniory, Y. Sun, A. W. Rost, V. Duppel, M. Krivenkov, S. Sheoran, P. Manuel, A. Varykhalov, B. Yan, R. K. Kremer, C. R. Ast, and B. V. Lotsch, Tunable Weyl and Dirac states in the nonsymmorphic compound CeSbTe, *Sci. Adv.* **4**, eaar2317 (2018).

[32] A. Topp, M. G. Vergniory, M. Krivenkov, A. Varykhalov, F. Rodolakis, J. L. McChesney, B. V. Lotsch, C. R. Ast, and L. M. Schoop, The effect of spin-orbit coupling on nonsymmorphic square-net compounds, *J. Phys. Chem. Solids* **128**, 296 (2019).

[33] S. Yue, Y. Qian, M. Yang, D. Geng, C. Yi, S. Kumar, K. Shimada, P. Cheng, L. Chen, Z. Wang, H. Weng, Y. Shi, K. Wu, and B. Feng, Topological electronic structure in the antiferromagnet HoSbTe, *Phys. Rev. B* **102**, 155109 (2020).

[34] K. Pandey, R. Basnet, A. Wegner, G. Acharya, M. R. U. Nabi, J. Liu, J. Wang, Y. K. Takahashi, B. Da, and J. Hu, Electronic and magnetic properties of the topological semimetal candidate NdSbTe, *Phys. Rev. B* **101**, 235161 (2020).

[35] B. Lv, J. Chen, L. Qiao, J. Ma, X. Yang, M. Li, M. Wang, Q. Tao, and Z.-A. Xu, Magnetic and transport properties of low-carrier-density Kondo semimetal CeSbTe, *J. Phys.: Condens. Matter* **31**, 355601 (2019).

[36] Y. Wang, Y. Qian, M. Yang, H. Chen, C. Li, Z. Tan, Y. Cai, W. Zhao, S. Gao, Y. Feng, S. Kumar, E. F. Schwier, L. Zhao, H. Weng, Y. Shi, G. Wang, Y. Song, Y. Huang, K. Shimada, Z. Xu *et al.*, Spectroscopic evidence for the realization of a genuine topological nodal-line semimetal in LaSbTe, *Phys. Rev. B* **103**, 125131 (2021).

[37] See Supplemental Material at <http://link.aps.org/supplemental/10.1103/PhysRevMaterials.6.L031201> for more information, which includes Refs. [38–42,45–50].

[38] P. Hohenberg and W. Kohn, Inhomogeneous electron gas, *Phys. Rev.* **136**, B864 (1964).

[39] W. Kohn and L. J. Sham, Self-consistent equations including exchange and correlation effects, *Phys. Rev.* **140**, A1133 (1965).

[40] P. E. Blöchl, Projector augmented-wave method, *Phys. Rev. B* **50**, 17953 (1994).

[41] G. Kresse and J. Furthmüller, Efficient iterative schemes for *ab initio* total-energy calculations using a plane-wave basis set, *Phys. Rev. B* **54**, 11169 (1996).

[42] G. Kresse and J. Furthmüller, Efficiency of ab-initio total energy calculations for metals and semiconductors using a plane-wave basis set, *Comput. Mater. Sci.* **6**, 15 (1996).

[43] Z. Ren, A. A. Taskin, S. Sasaki, K. Segawa, and Y. Ando, Large bulk resistivity and surface quantum oscillations in the topological insulator $\text{Bi}_2\text{Te}_2\text{Se}$, *Phys. Rev. B* **82**, 241306(R) (2010).

[44] A. A. Taskin, Z. Ren, S. Sasaki, K. Segawa, and Y. Ando, Observation of Dirac Holes and Electrons in a Topological Insulator, *Phys. Rev. Lett.* **107**, 016801 (2011).

[45] J. P. Perdew, K. Burke, and M. Ernzerhof, Generalized Gradient Approximation Made Simple, *Phys. Rev. Lett.* **77**, 3865 (1996).

[46] S. L. Dudarev, G. A. Botton, S. Y. Savrasov, C. J. Humphreys, and A. P. Sutton, Electron-energy-loss spectra and the structural stability of nickel oxide: An LSDA+U study, *Phys. Rev. B* **57**, 1505 (1998).

[47] H. J. Monkhorst and J. D. Pack, Special points for Brillouin-zone integrations, *Phys. Rev. B* **13**, 5188 (1976).

[48] M. P. L. Sancho, J. M. L. Sancho, J. M. L. Sancho, and J. Rubio, Highly convergent schemes for the calculation of bulk and surface Green functions, *J. Phys. F: Met. Phys.* **15**, 851 (1985).

[49] A. A. Mostofi, J. R. Yates, G. Pizzi, Y.-S. Lee, I. Souza, D. Vanderbilt, and N. Marzari, An updated version of wannier90: A tool for obtaining maximally-localised Wannier functions, *Comput. Phys. Commun.* **185**, 2309 (2014).

[50] Q. Wu, S. Zhang, H.-F. Song, M. Troyer, and A. A. Soluyanov, WannierTools: An open-source software package for novel topological materials, *Comput. Phys. Commun.* **224**, 405 (2018).

[51] K. Pandey, D. Mondal, J. W. Villanova, J. Roll, R. Basnet, A. Wegner, G. Acharya, M. R. U. Nabi, B. Ghosh, J. Fujii, J. Wang, B. Da, A. Agarwal, I. Vobornik, A. Politano, S. Barraza-Lopez, and J. Hu, Magnetic topological semimetal phase with electronic correlation enhancement in SmSbTe, *Adv. Quantum Technol.* **4**, 2100063 (2021).